Assessing Urban Methane Emissions using Column Observing Portable FTIR Spectrometers and a Novel Bayesian Inversion Framework

Taylor S. Jones[1,2], Jonathan E. Franklin[1], Jia Chen[3], Florian Dietrich[3], Kristian D. Hajny[4], Johannes C. Paetzold[3], Adrian Wenzel[3], Conor Gately[1,2], Elaine Gottlieb[1], Harrison Parker[5,6], Manvendra Dubey[5], Frank Hase[7], Paul B. Shepson[4], Levi H. Mielke[8], and Steven C. Wofsy[1]

[1]School of Engineering and Applied Sciences, Harvard University
[2]Department of Earth and Environment, Boston University
[3]Environmental Sensing and Modeling, Technical University of Munich (TUM), Munich, Germany
[4]Purdue University
[5]Los Alamos National Laboratory
[6]California Institute of Technology
[7]Karlsruhe Institute of Technology
[8]University of Indianapolis

Correspondence: Taylor Jones (tsjones@bu.edu)

Abstract.

Cities represent a large and concentrated portion of global greenhouse gas emissions, including methane. Quantifying methane emissions from urban areas is difficult, and inventories made using bottom-up accounting methods often differ greatly from top-down estimates generated from atmospheric observations. Emissions from leaks in natural gas infrastructure are difficult to predict, and are therefore poorly constrained in bottom-up inventories. Natural gas infrastructure leaks and emissions from end uses can be spread throughout the city, and this diffuse source can represent a significant fraction of a city's total emissions.

We investigated diffuse methane emissions of the city of Indianapolis, USA during a field campaign in May of 2016. A network of five portable solar-tracking Fourier transform infrared (FTIR) spectrometers was deployed throughout the city. These instruments measure the mole fraction of methane in a total column of air, giving them sensitivity to larger areas of the city than in situ sensors at the surface.

We present an innovative inversion method to link these total column concentrations to surface fluxes. This method combines a Lagrangian transport model with a Bayesian inversion framework to estimate surface emissions and their uncertainties, together with determining the concentrations of methane in the air flowing into the city. Variations exceeding 10 ppb were observed in the inflowing air on a typical day, somewhat larger than the enhancements due to urban emissions (<5 ppb downwind of the city). We found diffuse methane emissions of $73(\pm22)$ $\mathrm{mol\,s^{-1}}$, about 50% of the urban total and 68% higher than estimated from bottom-up methods, albeit somewhat smaller than estimates from studies using tower and aircraft observations. The measurement and model techniques developed here address many of the challenges present when quantifying urban greenhouse gas emissions, and will help in the design of future measurement schemes in other cities.

1 Introduction

Methane (CH$_4$) is a powerful greenhouse gas that is emitted to the atmosphere from both anthropogenic and natural sources (Montzka et al., 2011). Urban areas, which represent the majority of global anthropogenic greenhouse gas emissions (Hopkins et al., 2016), contain a mix of sources of methane, including landfills, industrial facilities, and fugitive emissions associated with natural gas infrastructure and end use. These fugitive emissions are a significant source of methane in some cities (Townsend-Small et al., 2012; McKain et al., 2015; Chen et al., 2020), but their detection and quantification is difficult (Phillips et al., 2013; Brandt et al., 2014). Governments have established goals for mitigating these emissions (Rosenzweig et al., 2010), creating a need for long term measurement systems to monitor progress and identify areas where action is needed (Gurney et al., 2015; Dietrich et al., 2020).

The relative contribution of these different types of sources can vary greatly from city to city. In the greater Boston region, one study concluded that 60 to 100% of methane emissions were due to leaks and inefficiencies in the natural gas sector. It was estimated that Boston's natural gas system had an overall emission rate of 2.1 to 3.3% of gas used in the region, much larger than a published national estimate of 1.1%. It was thought that these large emissions were likely attributable to aging cast iron and bare steel pipelines (McKain et al., 2015). A contrasting example would be the emissions profile of Indianapolis, Indiana, where only 24 km out of 6521 km of pipelines are cast iron, with the vast majority being newer plastic and protected steel (Lamb et al., 2016; Von Fischer et al., 2017). Indianapolis also has large point sources in the city, such as landfills, which result in an estimated natural gas sector contribution ranging from 21 to 69% of total urban emissions (Cambaliza et al., 2015; Lamb et al., 2016; Maasakkers et al., 2016; Balashov et al., 2020). Even in cities with modern infrastructure, diffuse emissions can still be a large percentage of the total urban methane budget, and accurate information about their magnitude is critical for those interested in mitigating the problem.

There are two basic methods to quantify the emission rate of a trace gas (such as methane) from an urban area. The first is the bottom-up approach, which starts by taking an inventory of the major point sources (e.g. landfills, compressor stations) and density of diffuse sources in the domain, and then applying emission factors to all of these sources to compute a total flux value. We consider any source with a known extent less than 1km x 1km (one grid cell in our model) to be a point source. Examples of bottom-up methane inventories available for the continental United States include EDGAR (European Commission, 2011), and the EPA gridded national inventory (Maasakkers et al., 2016).

The other approach to the quantification of emissions is the top-down method, where atmospheric measurements are made, and the emission rate is derived from these observations. Top-down methods that have been successfully used to constrain urban methane emissions include aircraft mass-balance techniques (Cambaliza et al., 2015), and inverse modeling approaches using in situ sensors mounted on towers (McKain et al., 2015) and/or aircraft (Peischl et al., 2013; Wennberg et al., 2017; Lopez-Coto et al., 2020). Currently, anthropogenic methane emission estimates from bottom-up and top-down methods can differ greatly at national (Miller et al., 2013) and urban (Lamb et al., 2016) scales, and improved methods in both approaches are needed in order to provide urban planners and lawmakers with the information they need to enact effective carbon policies (Duren and Miller, 2012). The goal of this paper is to quantify diffuse methane emissions from an urban area with improved natural gas

infrastructure (Indianapolis) on a city-wide scale using a small network of total column sensors. We focus on diffuse emissions here because these have been proven to be the most difficult to quantify, and the major point sources in Indianapolis are few and relatively well characterized. In order to accomplish this, solutions to several measurement and modeling challenges must be devised. These challenges include relatively low signal-to-noise levels and difficulty in determining the background concentration of methane in the air entering the city. A rigorous analysis of the errors involved is also critical to the success of the project.

Satellite observations of methane have been used in inverse modeling estimates of methane emissions (Bergamaschi et al., 2009), however current generation satellites lack the resolution needed to resolve emissions on urban scales (Turner et al., 2018). Past and current spaceborne methane instruments include SCIAMACHY (Bovensmann et al., 2002) (2003-2012) which was resolved at 30 km $\times$ 60 km, and GOSAT (Kuze et al., 2009) (2009-present) which has 10 km diameter pixels. The latest major satellite with methane measurement capabilities, TROPOMI (Veefkind et al., 2012; Hu et al., 2018), is able to resolve 5.6 $\times$ 3.5 km pixels across the globe. Several methane observing satellites with higher spatial resolution are currently being developed (Jacob et al., 2016), but their ability to resolve emissions from cities is unknown, and efforts to quantify urban emissions from space will require extensive calibration and validation with ground-based and aircraft-based measurements.

1.1 EM27/SUN Spectrometers

The Bruker model EM27/SUN is a compact, solar-tracking total column Fourier transform infrared (FTIR) spectrometer (Gisi et al., 2012; Hase et al., 2016). These instruments record high-resolution solar spectra in a near-infrared window that includes strong absorption features for CO_2, CH_4, CO, H_2O, and O_2. Using retrieval algorithms developed for the Total Column Carbon Observing Network (TCCON, Wunch et al. (2011)), the EM27/SUN can be used to compute the total column concentrations of these gases every 6 seconds during sunlit hours (Chen et al., 2016; Hedelius et al., 2016). The retrieval product is total-column dry air mole fraction of methane (denoted XCH_4, units of parts-per-billion) which represents what the mole fraction of methane in the column would be if water vapor was removed. EM27/SUN sensors have been calibrated alongside TCCON instruments, which are themselves calibrated against WMO in situ standards.

Using a surface-based total column sensor offers some advantages over in situ (direct sampling) methods. Since they sample an entire column of air, they do not need to be mounted on towers or tall buildings in order to measure methane aloft, and they are sensitive to emissions from an extended area of the city (Wu et al., 2018). Hence the EM27/SUN can be deployed and relocated quickly and inexpensively, while still adequately sampling the desired emission sources. Using multiple EM27/SUNs in an upwind-downwind configuration has been proven to be an effective way to measure methane emissions from dairy farms (Chen et al., 2016; Viatte et al., 2017) and coal mining areas (Luther et al., 2019), and some work has explored their usefulness in cities (Hase et al., 2015; Chen et al., 2020; Dietrich et al., 2020). There is also a coordinated effort to build a world wide network of these sensors (Frey et al., 2019). These spectrometers have also been used to make observations of carbon emissions from individual sources such as power plants (Toja-Silva et al., 2017) and volcanoes (Butz et al., 2017). Some work has even been done to take column measurements from moving platforms (Klappenbach et al., 2015; Kille et al., 2017). The sensitivity of these instruments enable them to detect small methane gradients across cities associated with fugitive emissions from natural

gas infrastructure. In this paper, a network of sensors was temporarily installed in the city of Indianapolis, in order to measure diffuse emissions identified in previous studies (Lamb et al., 2016). Total column sensors measure absorption spectra using the sun as a source, and therefore cannot be used at night or in overcast situations, but they can operate well in partly cloudy conditions.

2 Methods

A field campaign in Indianapolis, Indiana was carried out in May of 2016. Methane emissions have already been characterized in Indianapolis by the INFLUX experiment (Lamb et al., 2016; Davis et al., 2017), using several years of in situ measurements from towers as well as aircraft observations. Indianapolis lacks complex terrain and has few large upwind methane point sources, which would make the transport modeling more difficult. Extensive work has also been done to characterize the methane concentrations of inflowing air entering Indianapolis (Balashov et al., 2020).

During the campaign, five EM27/SUN spectrometers (designated *ha, hb, kf, ma,* and *pi*) were deployed throughout the city for five days of measurement. Four of the sensors were set up in fixed locations throughout the campaign, while one unit (*pi*) was moved from day-to-day, based on wind forecasts, to maximize sensitivity to urban emissions.

2.1 Spatial Distribution of Fluxes

The largest single source of methane emissions in Indianapolis is the South Side landfill (SSLF), which emits methane at a rate of 28 to $45\,\mathrm{mol\,s^{-1}}$ (Cambaliza et al., 2015; Lamb et al., 2016; Maasakkers et al., 2016; Balashov et al., 2020). Three other landfills, which are outside of the city limits but inside the domain of this study, are the Twinbridges Landfill ($17.5\,\mathrm{mol\,s^{-1}}$), the Caldwell Landfill ($8.5\,\mathrm{mol\,s^{-1}}$), and the Noblesville Landfill ($0.1\,\mathrm{mol\,s^{-1}}$). The city's main waste water treatment facility, located near the SSLF, is also a notable methane source, with an estimated emission rate of 3 to $7\,\mathrm{mol\,s^{-1}}$. Natural gas is supplied to the city via the Panhandle Eastern Pipeline which runs from Oklahoma to Michigan. The connection point between this pipeline and the municipal pipeline grid is known as the city gate (CG) and is also a potential methane point source. Emissions from the CG are estimated at $1\,\mathrm{mol\,s^{-1}}$ (Balashov et al., 2020).

Additional sources of methane emissions are leaks in the city's natural gas infrastructure, venting, and inefficiencies in natural gas combustion downstream. These sources are spread throughout the city and referred to as diffuse emissions, and have been estimated to account for an additional 20 to $64\,\mathrm{mol\,s^{-1}}$, or 21 to 69% of total methane emissions (Lamb et al., 2016). Lamb et al. modeled the diffuse source on a $1 \times 1\,\mathrm{km^2}$ grid, spatially distributed based on HESTIA emissions of CO_2 from natural gas combustion (Gurney et al., 2012). This approach was taken because high resolution methane inventories are not available, and because the location of fugitive emissions could plausibly be correlated with sites of combustion. This distribution is also shown in Figure 1.

The resulting gridded emissions product, F, is a function of longitude (x), latitude (y), and emissions sector (s). This spatial distribution was used in previous work constraining methane fluxes in Indianapolis using tower-based sensors (Lamb et al., 2016), as shown in Figure 1 and described in Table 1. Emissions were ultimately grouped into four sectors. We have chosen to
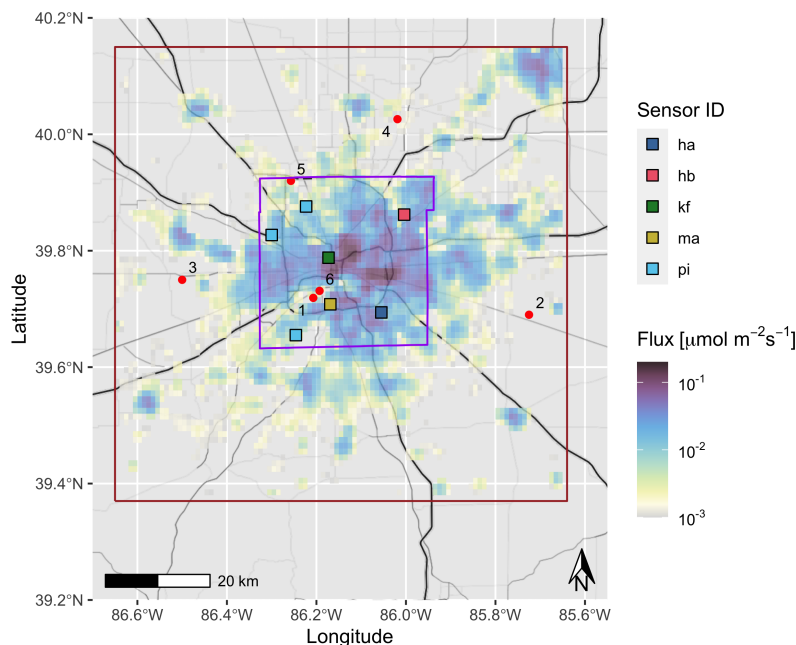
Figure 1. Prior estimate of emissions due to natural gas infrastructure. EM27/SUN deployment locations are shown with squares. Locations of known point sources are also shown (red circles, summarized in Table 1). The study domain is shown in brown, and the boundary of Marion County is shown in purple. Map tiles by Stamen Design, under CC BY 3.0. Data by OpenStreetMap, © OpenStreetMap contributors 2020. Distributed under the Open Data Commons Open Database License (ODbL) v1.0

120   define sectors based on the Intergovernmental Panel on Climate Change (IPCC) guidelines (IPCC, 2006). The first three sectors of interest in Indianapolis, and their corresponding IPCC abbreviations, are: diffuse fugitive emissions (1B) , landfills (6A), and the waste water treatment (6B). The forth sector, the city gate, is abbreviated CG. The city gate also falls into IPCC category 1B, but was treated seperately for this study as it is a significant point source. Although some works have used EM27/SUN observations to constrain fluxes from point sources (Toja-Silva et al., 2017), the sensors in this experiment were spread across

125   the city to maximize sensitivity to diffuse emissions. The locations of the point sources and sensors are given in Tables 1 and 2, and shown in Figure 1, which also shows the extent of the study domain.

2.2 EM27/SUN Calibration

Absolute calibrations of EM27/SUN spectrometers have been performed by comparing measurements to co-located TCCON stations (Frey et al., 2019; Hedelius et al., 2016). However, when using a multiple sensor network, relative calibrations between

130   instruments have proven to be sufficiently precise and to have minimal drift over time (Chen et al., 2016; Frey et al., 2019). To obtain relative calibrations, two additional days of data were taken: one before and one after the field deployments. On these calibration days, all five sensors were placed next to each other to ensure that they all measured the same air mass. The relative

Table 1. Location and estimated methane flux of major point sources in Indianapolis.

	Point Source	Flux	Latitude (° N)	Longitude (° E)
1	South Side Landfill	45.0	39.719	-86.207
2	Caldwell Landfill	8.5	39.690	-85.725
3	Twinbridges Landfill	17.5	39.750	-86.500
4	Noblesville Landfill	0.1	40.026	-86.019
5	Pipeline City Gate	1.0	39.920	-86.257
6	Wastewater Treatment	5	39.731	-86.193

Fluxes are given in $\mathrm{mol\,s^{-1}}$. Adapted from (Lamb et al., 2016)

Table 2. Location of EM27/SUNs on each day of the campaign. All instruments were operated at ground level, except for *hb*, which was on top of a 20 meter building.

Instrument	Date(s)	Latitude (° N)	Longitude (° E)	Operator
ha	all	39.694	-86.055	Harvard University
hb	all	39.862	-86.004	Harvard University
ma	all	39.708	-86.173	Technical University of Munich
kf	all	39.788	-86.173	Technical University of Munich
pi	5/13, 5/15, 5/18	39.827	-86.300	Los Alamos National Lab
pi	5/19	39.655	-86.246	-
pi	5/22	39.876	-86.223	-

offset between sensors is stable, and our studies have shown that this type of calibration results in a relative XCH$_4$ precision between instruments of 0.2 ppb when using an averaging time of 10 minutes (Chen et al., 2016). The offset calibration data are shown in Figure 2.

Ahead of the campaign we noted increasing degradation of the solar tracking mirrors for sensors *ha* and *hb*. Our calibration data showed slowly varying deviations in the derived XCO$_2$ and XCH$_4$ values of these two instruments relative to the remaining three sensors, and these deviations were correlated with the derived fractional variation in solar intensity which quantifies the DC signal of the interferogram. The XCO$_2$ and XCH$_4$ variations were thus attributed to optical imperfections. This correlation enabled us to perform an empirical correction which has been applied to all *ha* and *hb* data in this study. In August 2016 new optics were installed, drift in these sensors vanished, and no further calibration was required.

2.3 Aircraft and LIDAR Observations

In addition to the total column measurements, four flights of Purdue University's Airborne Laboratory for Atmospheric Research (ALAR) aircraft were performed during the course of the campaign. These flights consisted of upwind and downwind
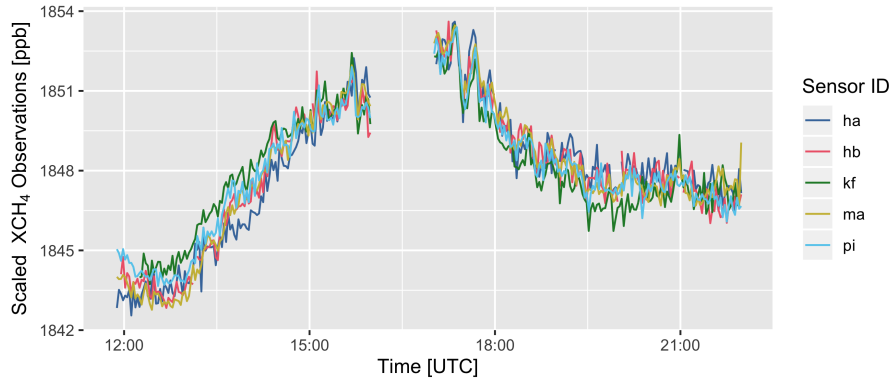
Figure 2. Total column dry mole fraction methane (XCH_4) for the five instruments on one of the two side-by-side inter-comparison days. Calibration scaling factors have been applied to this data.

145   transects of the city, as well as spirals in strategic locations. The ALAR was equipped with a Picarro model G2301-f cavity ringdown spectrometer (Crosson, 2008) which measured dry CO_2 and CH_4 concentrations in situ. High frequency wind speed and direction data was also measured on the ALAR using the Best Air Turbulence (BAT) probe (Garman et al., 2006). Continuous wind measurements, as well as the the height of the top Planetary Boundary Layer (PBL), were monitored throughout the campaign using a wind doppler lidar co-located with *hb* (Bonin et al., 2018). Although wind speeds and wind directions

150   derived from the lidar data are less accurate than those from the aircraft, they still have utility in verifying the stability of the atmosphere and the accuracy of wind forecasts throughout the day. The ALAR wind data were used to compute daily wind error statistics, which were then used in the uncertainty calculations of our final results. ALAR and lidar data from throughout the campaign are shown in the supporting information.

2.4   Transport Model

155   The Stochastic Time-Inverted Lagrangian Transport (STILT) model (Lin, 2003; Fasoli et al., 2018) was used to compute the sensitivity of the total column observations to surface emissions. The model simulates the movement of non-reactive trace gases by computing the trajectories of hypothetical massless particles released from the observation location, and advected and diffused backwards in time according to a gridded meteorological product. For this work, the NAMS-12km product (Janjic and Gall, 2012) was used.

160   A linear model $\mathbf{A}$ can be created to relate emissions to our column observations.

$$\Delta\mathbf{y} = \mathbf{A}\mathbf{a_s} + \varepsilon_a \tag{1}$$

Here the enhancement in the column due to emissions in the urban area is denoted $\Delta\mathbf{y}$. The vector $\mathbf{a_s}$ consists of scaling factors for each sector. The matrix $\mathbf{A}$ contains the products of Lagrangian footprints, f, and a priori emissions fluxes, F. Error in the model due to uncertainties in the footprint values and observations is represented by the ε_a term.

The footprint as a function of location (x, y) and release time (t) can be expressed as:

$$f(x, y, t) = \frac{m_{air}}{h(t)\bar{\rho}(x, y, t)} \frac{1}{N_p} \sum_{i=1}^{N_p} \Delta t_i(x, y) \qquad (2)$$

where m_{air} is the mean molar mass of air ($29\,\mathrm{g\,mol^{-1}}$), $\bar{\rho}$ is the mean density of the air at coordinate (x, y, t) and N_p is the number of particles released. Δt_i is the amount of time particle i spent in coordinate (x, y), and h is the height of the mixing layer, which is typically defined as half of the height of the PBL (Lin, 2003). The value of h is adjusted in the time steps immediately before the particle release to account for the time needed for these particles to vertically mix into the boundary layer (Fasoli et al., 2018).

In order to create slanted total column STILT footprints, model particles are released at altitudes of 25, 50, 75, 100, 150, 200, 300, 400, 600, 800, 1000, 1500, 2000, and 2500 meters relative to the instrument location. These altitudes were chosen to be dense near the surface and more sparse nearer the top of the boundary layer. Particle releases at higher altitudes are not needed, as air significantly above the boundary layer does not interact with ground emissions on the scale of our domain.

Since the observed air mass is a slanted column with variable azimuth and solar elevation during the day (Hase et al., 2016), the latitude and longitude of the particle releases were adjusted based on the solar zenith and azimuth angles at the time of the release. We released 1000 particles from each level every 15 minutes. To create the total column footprint, f_c, footprints from the $L = 14$ different altitudes are combined using a pressure weighting function, $w(z)$. The weighting of the footprints can also be affected by the observing system's averaging kernel ($A_k(z)$), which is the relative sensitivity to concentrations at different altitudes. Since the averaging kernel of the EM27/SUN XCH$_4$ retrieval is ≈ 1 in the lower troposphere (Hedelius et al., 2016), this effect is minimal.

$$f_c(x, y, t) = \sum_{i=1}^{L} w(z_i) A_k(z_i) f_i(x, y, t) \qquad (3)$$

This is similar to the "XSTILT" method for constructing STILT footprints for satellite observations (Wu et al., 2018). A more detailed description of this pressure weighting scheme is in the supplemental information. An example total column footprint is shown in Figure 3.

The column footprints are then multiplied by the a priori emissions field $F(x, y, s)$ and summed to produce a row n in the matrix $\mathbf{A}$ at the time step m. F is a function of latitude, x, longitude, y, and emissions sector, s, but is not temporally resolved. The resulting matrix $\mathbf{A}$ will have a number of columns equal to the number of observation time points being simulated and a number of rows equal to the number of emission sectors in the inventory.

$$\mathbf{A}_{m,n} = \sum_{i=1}^{N_x} \sum_{j=1}^{N_y} f_c(x_i, y_j, t_m) F(x_i, y_j, s_n) \qquad (4)$$

Equation 4 represents the expected column-averaged methane enhancement at each measurement point in time due to urban methane emissions given an emissions field of dimension $N_x \times N_y$. The values of $\mathbf{A}$ for the observations of May 13 are shown
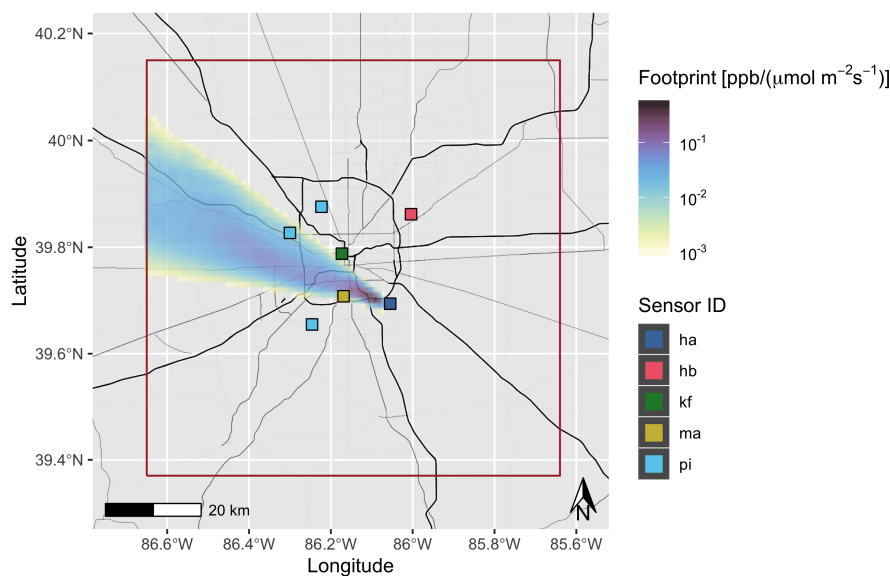
Figure 3. Total column footprint for sensor *ha* on 05/13/2016 at 12:30 UTC. The prevailing wind direction was from WNW, which resulted in *ha* being downwind of the city. Map tiles by Stamen Design, under CC BY 3.0. Data by OpenStreetMap, © OpenStreetMap contributors 2020. Distributed under the Open Data Commons Open Database License (ODbL) v1.0

in Figure 4. It is important to note that these prior expected enhancements are completely dependent on the prior emissions map and footprint values, and are not influenced by any XCH$_4$ observations.

2.5 Background Methane Concentrations

Air entering the city has total column methane concentrations in excess of 1800 ppb, which can vary in time and space. The seasonal cycle is roughly ± 20 ppb, and latitude gradients across the Northern Hemisphere are roughly 50 ppb (Parker et al., 2011). Global mean XCH$_4$ is currently increasing at a rate of 7.6 (±0.4) ppb every year (Zhou et al., 2018), although the rate of increase of mean methane concentrations has not been consistent over the past few decades (Turner et al., 2019). As air moves over the continent, it can also entrain additional methane from emissions hundreds of kilometers upwind of the urban area of interest. The concentration of methane in the inflowing air ("background"), represents >99% of the methane observed in the total column, therefore variations in background concentrations during the experiment must be very accurately characterized.

Previous work which studied background methane concentrations in Indianapolis showed significant variations in the amount of methane in inflowing air and stressed the importance of carefully accounting for this effect (Balashov et al., 2020). Previous flux inversions of methane and other trace gases have dealt with the background in different ways. Many works have made an assumption that measurements from a sensor that is nominally upwind represents the inflowing air (McKain et al., 2015;
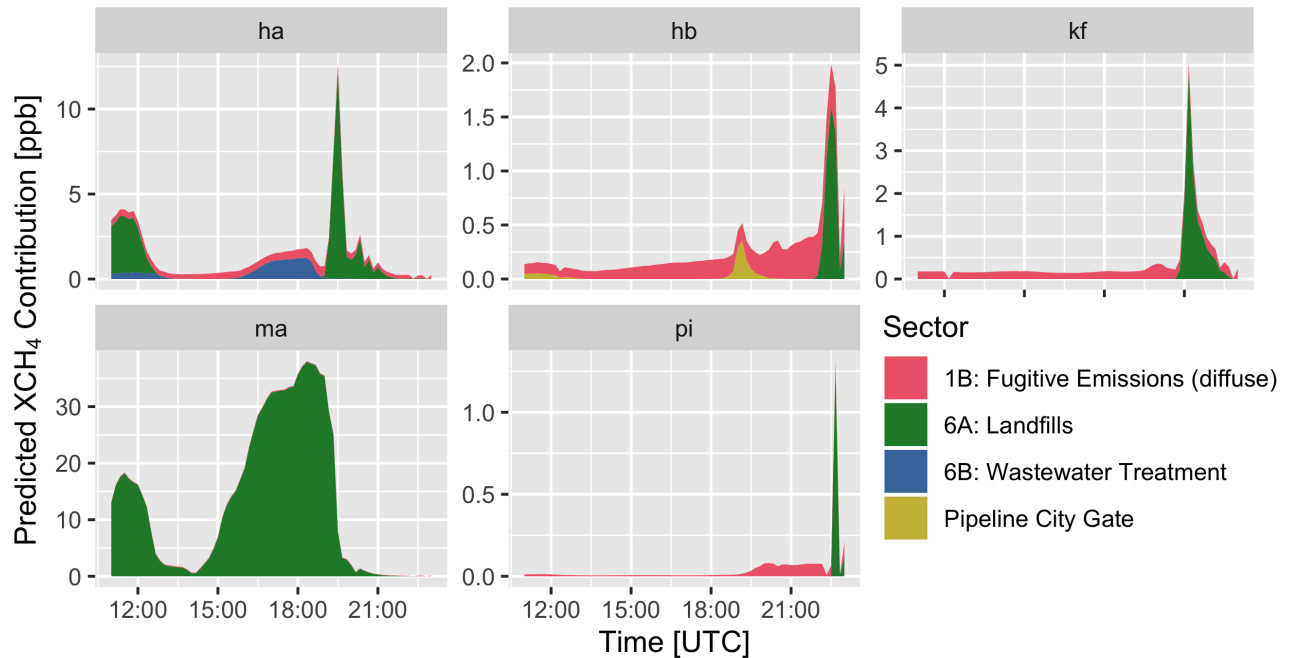
Figure 4. Predicted XCH$_4$ Contribution to each measurement from each source for May 13. These values are computed by multiplying the STILT footprints by the a priori inventory.

Lamb et al., 2016; Chen et al., 2016; Sargent et al., 2018). In this work, however, a background time series is modeled using all of the network data. This additional step is required because of significant variations observed in the background over short time scales (<1 hour). The background time series vector (**b**) represents the mean total column methane concentration along the domain boundary every 15 minutes, starting from the time when the first STILT particle enters the domain. The total column concentration is therefore modeled as the sum of the background entering the domain and the enhancement due to local emissions.

$$\mathbf{y} = \mathbf{A}\mathbf{a_s} + \mathbf{B}\mathbf{b} + \varepsilon_a + \varepsilon_b \tag{5}$$

Here **B** is the background influence matrix (BIM) which relates every observation to a distribution of influence from each background time point. Matrix **B** is unitless, as it merely transforms values from the boundary background ($mathbfb$, ppb) to background values at each observation point (also in parts per billion). An additional error term, ε_b, represents error (in ppb) in the background due to uncertainties in the BIM. It is important to note that because the values of the error terms ε_a and ε_b are unknown, and can be quite large, a careful statistical inversion must be performed to retrieve valid estimates of emissions. The

220   construction of $\mathbf{B}$ occurs during the computation of the STILT footprints. After defining the box that constitutes the edge of the domain, STILT particles are tracked backwards in time, and the time at which they cross the domain boundary is recorded. The relative influence of background air of different ages on observations at different sites is shown in Figure 5, and the BIM of *hb* for the first measurement day (May 13) is shown in Figure 6.

    The particle releases used to create the BIM are the same as those used to create the footprints described earlier, and so are

225   from 14 different altitudes up to 2500 meters. Transport is not modelled above this level is not modeled, which means there is a possibility that plumes present in the mid-troposphere will not be accounted for effectively.
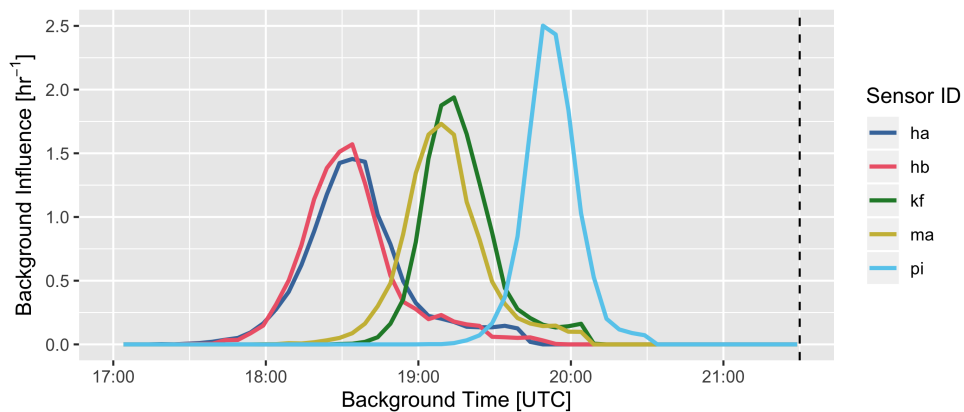
Figure 5. Fraction of background influence for all sites on May 13 at 21:30 UTC. Although entries in the BIM are unitless, here they are shown divided by the background time step. These are therefore residence time probability density functions, with the integrals over the graphs each equal to 1.

We can combine these linear operators into a single jacobian, $\mathbf{K}$, which allows us to treat the entire measurement, emission, transport, and background model as a single linear system.

$$\mathbf{K} = [\mathbf{A} \, \mathbf{B}] \tag{6}$$

230   The emissions scaling factors and domain background are then combined into a single state vector ($\mathbf{x}$).

$$\mathbf{x} = \begin{bmatrix} \mathbf{a_s} \\ \mathbf{b} \end{bmatrix} \tag{7}$$

$$\mathbf{y} = \mathbf{Kx} \tag{8}$$
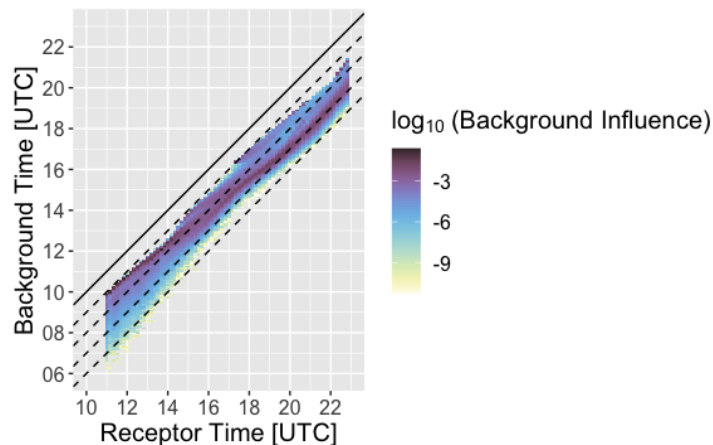
Figure 6. Background Influence Matrix (BIM) for instrument *hb* for the May 13 measurement day. The solid line is one-to-one, and represents a residence time of 0 hours within the modeling domain. The dashed lines represent residence times of 1, 2, 3, and 4 hours within the modeling domain.

2.6 Model Uncertainty

There are four main components to the uncertainty of the measurement-model system: background error (discussed previously), instrument measurement error, transport error, and source distribution error. The uncertainty of the EM27/SUN itself is taken from previous studies, and assumed to be 0.2 ppb at 10 minute integration times (Chen et al., 2016). The transport error is the uncertainty (in ppb) of a modeled total column observation due to uncertainties in the wind direction and wind speed used in the transport model. Using the ALAR observations, the relative wind errors could be computed. These calculations are shown in the supplemental information. The results from the wind error analysis are shown in Table 3.

The method for determining the transport error associated with each observation is based on previous work addressing uncertainties in STILT (Lin and Gerbig, 2005; Fasoli et al., 2018), however some major adjustments had to be made because of the nature of the domain in this study. A detailed description of this modified uncertainty calculation method can be found in the supplemental information. The transport error analysis also allowed us to predict the likelihood that a given observation was influenced by any of the known point sources. If footprints with point source influence were not removed, it would be difficult to detect the diffuse source contribution. Methane enhancements due to concentrated emissions on the edge of a footprint are difficult to model accurately, so we developed a meticulous procedure to screen out footprints that could be influenced by our designated large point sources, as follows:

1. A STILT simulation (with 1000 particle releases at each of 14 altitudes) is performed.

2. Wind speed and direction statistics are established, and 500 transport error simulations are performed (see supplemental information).

Table 3. Mean and standard deviations of wind speed and wind direction differences between the NAMS model winds and observations from the ALAR aircraft and the wind lidar. Negative values indicate that the NAMS model value is greater than the observation. The ALAR-NAMS standard deviations for each day were used in the transport error analysis.

| | Wind Speed Model Mismatch ($\mathrm{m\,s^{-1}}$) | | | | Wind Direction Model Mismatch (°CW) | | | |
| | Mean | | Std. Dev. | | Mean | | Std. Dev. | |
Date	Lidar	Aircraft	Lidar	Aircraft	Lidar	Aircraft	Lidar	Aircraft
05/13	-3.4	-0.2	6.5	2.2	-39.2	-3.3	59.0	16.4
05/15	2.3	1.0	6.7	1.5	-23.3	2.1	32.8	11.4
05/18	-0.9	0.2	4.1	1.6	30.5	5.8	66.5	20.9
05/19	0.7	-0.3	2.4	2.0	-14.5	0.6	46.9	23.4
05/22	-1.3	-	3.7	-	36.2	-	42.0	-
mean	-0.5	0.2	4.7	1.8	-2.06	1.3	49.4	18.0

3. Simulations where at least 10% of the expected methane enhancement are due to the known point sources (i.e. landfills, the waste water treatment plant, or the city gate) are deemed to have point source contribution.

4. The likelihood of point source influence is then defined as the percentage of simulations that meet this criterion.

5. Observations which have a likelihood of point source influence above a 50% threshold are not included in the analysis of diffuse emissions.

The results of this threshold technique for the five days of the campaign are shown in Figure 7. For example, more than 90% of the observations from instrument *ma* were influenced by the nearby South Side Landfill on three of the five days. The wind direction was different for the other two days: May 18 and May 19 (see supplemental information). Some of the observations from site *ha* on May 13 and May 15 also had to be discarded, as that sensor saw occasional influence from both the landfill and the waste water treatment plant.

The computed uncertainties in the total column methane concentration due to horizontal transport error are shown in Figure 8. Locations upwind of the city, such as *pi* on May 13 and May 15, have a much lower value than downwind sites even though they are experiencing the same amount of wind error. This is because the emissions upwind of *pi* (but still inside the domain) on these days are both weak and spread out, which means that shifts in the wind direction do not greatly affect the amount of methane observed at this location. This analysis gives us the ability to weight observations differently based on this error when computing the mean rate of urban emissions.

2.7 Uncertainties in Diffuse Emission Distribution

Diffuse emissions were assumed to be distributed around the urban area using a method based on the high resolution HESTIA database. To test the sensitivity of the inversion to this distribution, two other distributions were also examined, shown in Figure
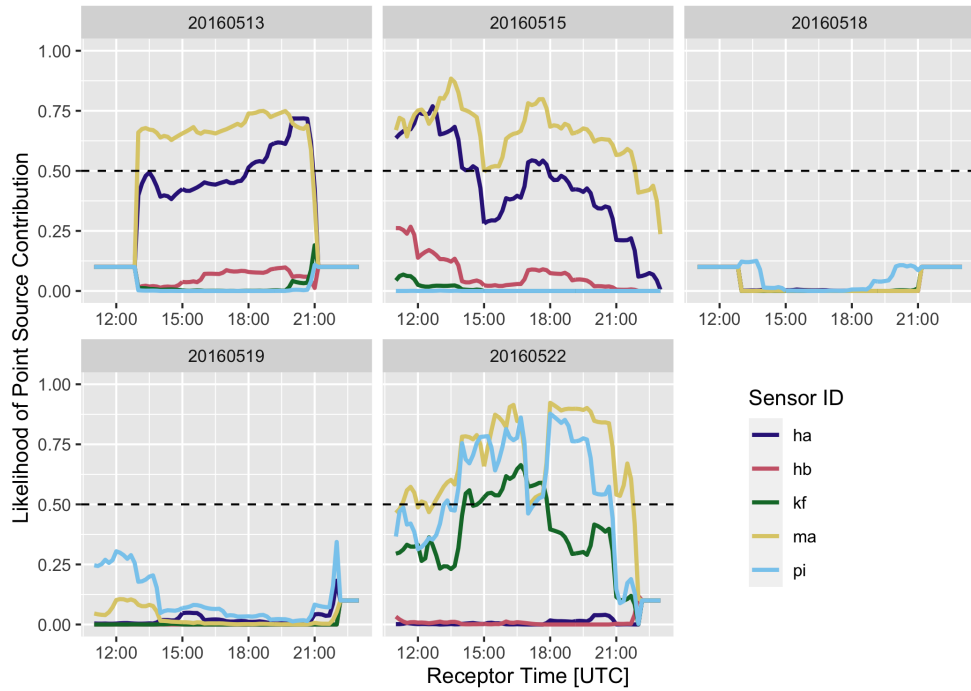
Figure 7. Likelihood of point source contribution for each site throughout the campaign. The threshold level, 50%, is shown in the dashed line.

270 9. The first partitions emissions based on population density, which can be assumed to be a proxy for the density of residential natural gas usage. If incomplete combustion and leakage are issues in household gas appliances, such as stoves and water/air heating systems, this could be a reasonable prior distribution of diffuse emissions. The second partitions emissions based on road density. Since urban natural gas pipes run underneath and along roads, this could be a reasonable prior for the distribution of leaks in pipes (Phillips et al., 2013). Both of these new inventories were scaled so that the total emissions from all three
275 methods were equal.
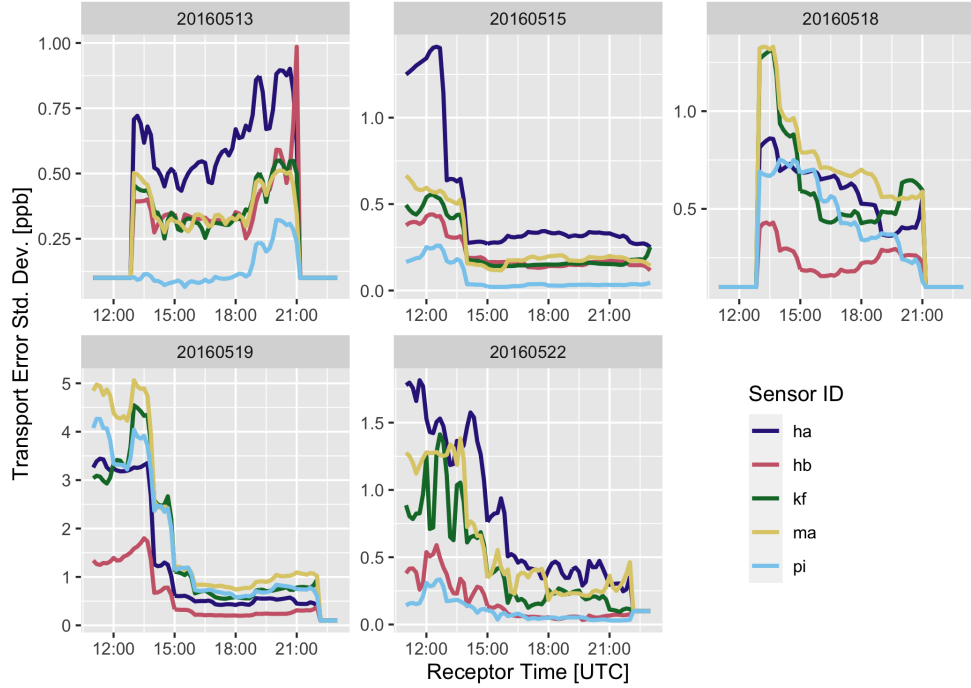
Figure 8. Standard deviations due to uncertainties in horizontal transport for the entire campaign.

2.8 Bayesian Framework

Uncertainties associated with the measurements, the prior estimate, and the transport model are all accounted for by using a linear Bayesian inversion framework (Rodgers, 2000). This method focuses on the reduction of a cost function, $\mathcal{J}(\mathbf{x})$, which weights the discrepancies between the model, observations, and prior estimates based on their uncertainties. If these uncertainties are assumed to be normally distributed, the log-likelihood cost function can be expressed as (Turner et al., 2018):

$$\mathcal{J}(\mathbf{x}) = \frac{1}{2}(\mathbf{Kx} - \mathbf{y})^{\mathbf{T}}\mathbf{S}_{\varepsilon}^{-1}(\mathbf{Kx} - \mathbf{y}) + \frac{1}{2}(\mathbf{x_a} - \mathbf{x})^{\mathbf{T}}\mathbf{S_a}^{-1}(\mathbf{x_a} - \mathbf{x}) \tag{9}$$

The prior state vector ($\mathbf{x_a}$) contains initial estimates of the scaling factors that for the emissions from each sector, as well as initial estimates of the background methane concentration at every relevant point in time. The entries corresponding to emissions scaling factors are all equal to 1, as the magnitude of the emissions map is the best a priori estimate of emissions.
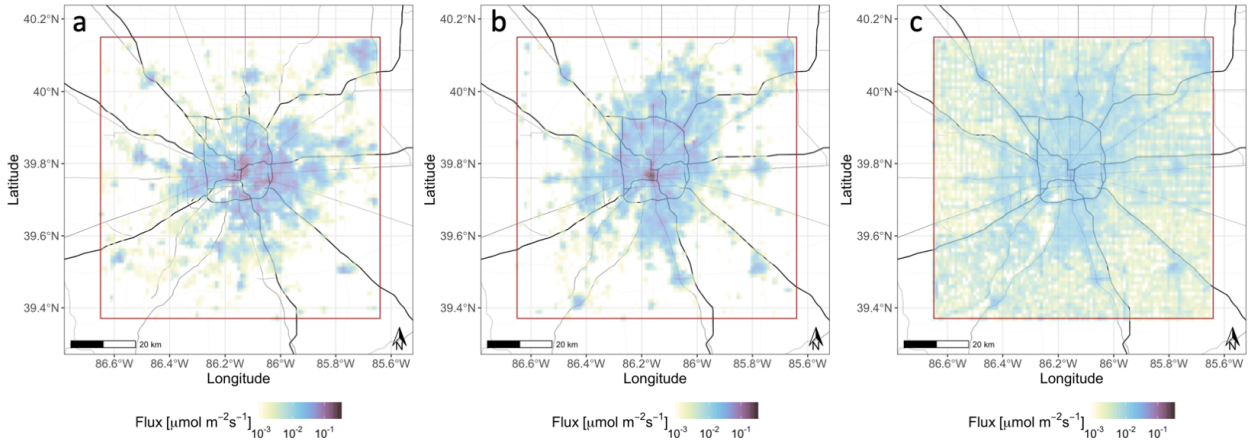
Figure 9. Diffuse emissions spatial distributions, based on (a) HESTIA, (b) population, and (c) road density. Map tiles by Stamen Design, under CC BY 3.0. Data by OpenStreetMap, © OpenStreetMap contributors 2020. Distributed under the Open Data Commons Open Database License (ODbL) v1.0

285 A background value of 1.84 ppm was chosen after a cursory look at the data. These values are not critical, as the framework assumes uninformed priors for all of the scaling factors and background values.

$$\mathbf{x_{ai}} = \begin{cases} 1, & 1 \le i \le n_{sec} & \textit{prior estimates of scaling factors} \\ 1.84, & \textit{otherwise} & \textit{prior estimates of boundary background in ppm} \end{cases} \tag{10}$$

where n_{sec} is the number of sectors. The first diagonal elements of the prior covariance structure $\mathbf{S_a}$ are the variances of the scaling factors of the emission sectors σ_s^2, and is chosen to be large ($\gg 1$). Having a weakly informative prior allows

290 the inversion to produce emission values that are dependent on the observations, while still relying on the spatial distribution

established by the prior. The remaining diagonal elements are the estimated uncertainties in the background estimate. These values are also chosen to be large, as the magnitude of the background signal is not known a priori.

$$\mathbf{S_{a_{i,j}}} = \begin{cases} \sigma_s^2, & i,j \leq n_{sec} \text{ and } i = j \quad \text{\textit{Variance of prior scaling factor estimates}} \\ 0, & i,j \leq n_{sec} \text{ and } i \neq j \quad \text{\textit{Assumed zero co-variance between sectors}} \\ \sigma_b^2 e^{-|\Delta t_{i,j}|/T_b}, & i,j > n_{sec} \quad \text{\textit{Background values co-vary with dependence of time between points}} \end{cases} \tag{11}$$

In Eq. 11, the amount of time, in hours, between observations i and j is represented by $\Delta t_{i,j}$. Most of the off-diagonal elements represent the correlation in errors between background concentrations, which is a function of how smoothly the background is expected to change. A background co-variance timescale (T_b) of 3 hours was used. This value was chosen so that synoptic and mesoscale wind patterns (Van Der Hoven, 1957) would be accounted for. Higher frequency (i.e. eddy scale) variations in wind speed are not accounted for in the NAMs model, so a shorter background co-variance time scale could not be used.

The model-observation covariance structure $\mathbf{S}_\varepsilon$ represents the total uncertainties of the transport model and the observations. The values of $\mathbf{S}_\varepsilon$ are dependent on factors such as uncertainties in the wind and heterogeneity of the prior emissions field. A modified version of the framework first described in Lin and Gerbig (2005) is used to compute the values for each observation. This framework requires estimations of standard deviations of wind speed, wind direction, and PBL height errors of the meteorology model, as well as correlation length-scales and time-scales for these errors. The length-scales for these types of errors are typically larger ($> 1\text{km}$) than the domain of interest in this study, so it is a reasonable assumption that the wind errors are completely correlated. The variance of the wind speed and wind direction errors were derived from the aircraft spiral observations as discussed in 2.6 and in the supporting information.

There exists an analytical solution for the cost function $\mathcal{J}(\mathbf{x})$, which is the maximum a posteriori (MAP) solution for the background time series and diffuse emissions scaling factor:

$$\hat{\mathbf{x}} = \mathbf{x_a} + \mathbf{G}(\mathbf{y} - \mathbf{K}\mathbf{x_a}) \tag{12}$$

Where $\mathbf{G}$ is the gain matrix:

$$\mathbf{G} = \mathbf{S_a}\mathbf{K^T}(\mathbf{K}\mathbf{S_a}\mathbf{K^T} + \mathbf{S}_\varepsilon)^{-1} \tag{13}$$

The uncertainties of the values of $\hat{\mathbf{x}}$ are computed by the construction of a posterior covariance matrix, $\mathbf{S_p}$, the diagonals of which describe the model framework's ability to reduce the uncertainties of the priors (Rodgers, 2000). It should be noted that this posterior will likely be dependant on the prior uncertainties chosen, and that a rigorous inversion should have reasonable prior estimates of error.

$$\mathbf{S_p} = (\mathbf{K^T}\mathbf{S}_\varepsilon^{-1}\mathbf{K} + \mathbf{S_a}^{-1})^{-1} \tag{14}$$
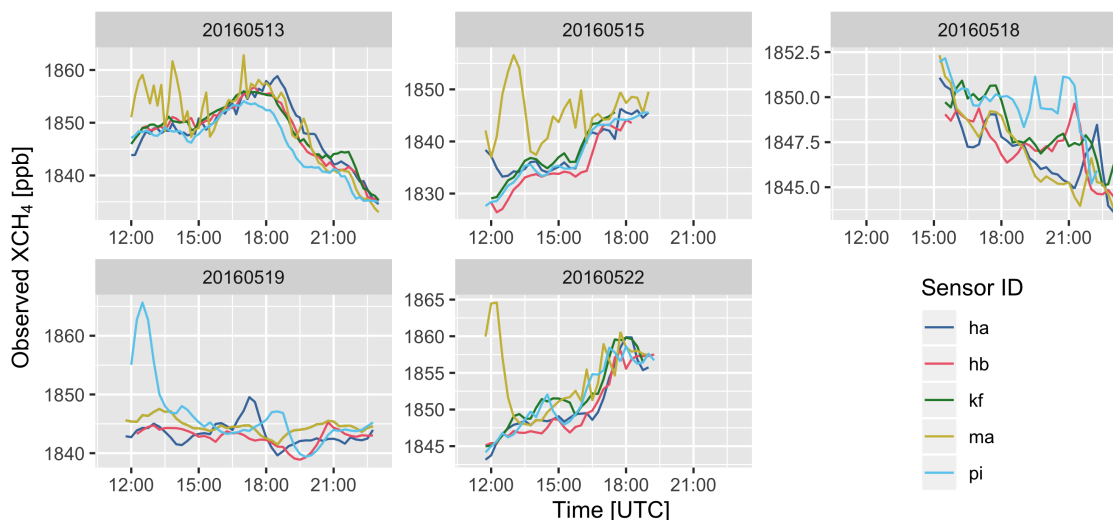
Figure 10. Total column dry mole fraction methane (XCH$_4$) for the five sensors on all five days of the campaign. The high frequency signal for sensor *ma* is due to its close proximity to the South Side Landfill, the largest point source in the city.

This formulation, like the above formula for $\hat{x}$, assumes that the prior has a Gaussian distribution (Turner et al., 2018).

3 Results

3.1 EM27/SUN Observations

Measured XCH$_4$ values (Figure 10) showed large variations throughout the day, in excess of 10 ppb on some of the days. Some of these variations propagate across the city from upwind to downwind locations, suggesting that these result from spatial and temporal variations present in the inflowing air and not due to emissions within the city. The gradients between sites were much smaller, on the order of 1 ppb across the city. The influence of the South Side Landfill, particularly on instrument *ma*, was evident in the form of high-frequency variations of 10-20 ppb. As noted above, the observations affected by landfill emissions were screened out of the inversion using the STILT footprints.

3.2 Inversion Results

The diffuse emissions scaling factors are summarized in Table 4. The model scaled the diffuse emissions from a prior value of 43.4 mol s^{-1} to a value of 73.3 ($\pm$ 22) mol s^{-1} with 95% confidence. The daily Bayesian inversions were able to adequately model background concentration time series that captured the dynamics of the plumes observed, including on May 13 when the background variation was the highest of all measurement days (Figure 11). The model was also able to fit the EM27/SUN

Table 4. Inversion results for the diffuse sector for all five days of the campaign. 95% confidence intervals are computed using the posterior error variances.

	Diffuse Emissions $(\mathrm{mol\,s^{-1}})$	C. I. $(\mathrm{mol\,s^{-1}})$	Fraction of Prior
prior	43.4	-	1
May 13, 2016	40.4	-23.4 to 103.2	0.93
May 15, 2016	146.3	67.2 to 225.4	3.37
May 18, 2016	-20.9	-83.2 to 41.4	-0.48
May 19, 2016	83.4	83.4 to 117.9	1.92
May 22, 2016	54.1	1.5 to 106.8	1.25
all days combined	73.3	51.5 to 95.1	1.69

observations very well (Figure 12). However, since most of the variation in XCH_4 was due to variation in the background, this fit does not represent the ability of the model to constrain emissions. The observed and modeled enhancements (Figure 13) give a clearer view of the emissions signal, which is small but clearly observable. In order to test the significance of the correlation between observed and modelled enhancements, points were binned in to 0.5 ppb wide bins based on model enhancement values. The mean observed enhancement values for the 0-0.5 ppb and 1-1.5 ppb bins were then tested to see if the were significantly distinct, resulting in a p-value of 0.003. This result suggests that even with such a small signal level, and in the presence of large background concentration variations, the model was able to detect and quantify enhancements in methane due to urban emissions.

Although we are confident that the model framework was able to detect meaningful methane fluxes using all five days of data, the daily inversions yield emission numbers that vary greatly and are sometimes non-physical, such as the negative emissions reported on May 18. This shows that a single day of measurements is unlikely to produce a robust result, and even the combination of all fives days should be viewed as an experimental proof-of-concept, and continuous measurements for many months should be used to produce a more compelling final emission number.
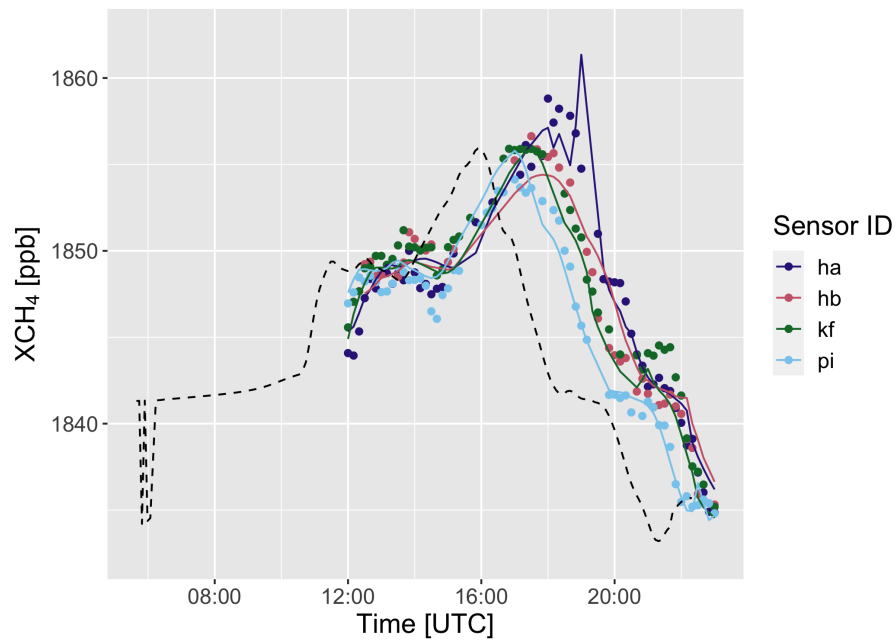
Figure 11. Observed XCH$_4$ values for May 13 (shown in points). Optimized domain boundary background values (gray, dashed) and optimized total column values, including urban emissions (colored lines) also shown.
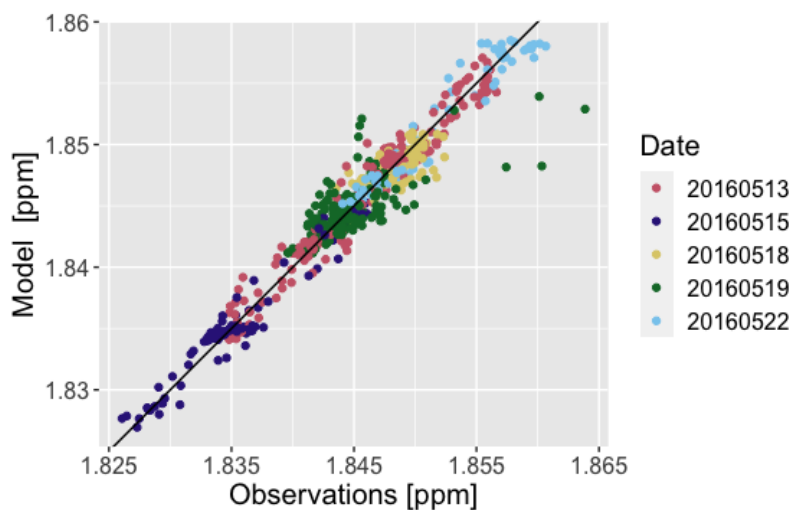
Figure 12. Optimized model correlation with the five days observations. The black curve is a 1-1 line. Each point represents a 15-minute average from a single sensor. Observations with significant point source influence have been removed.
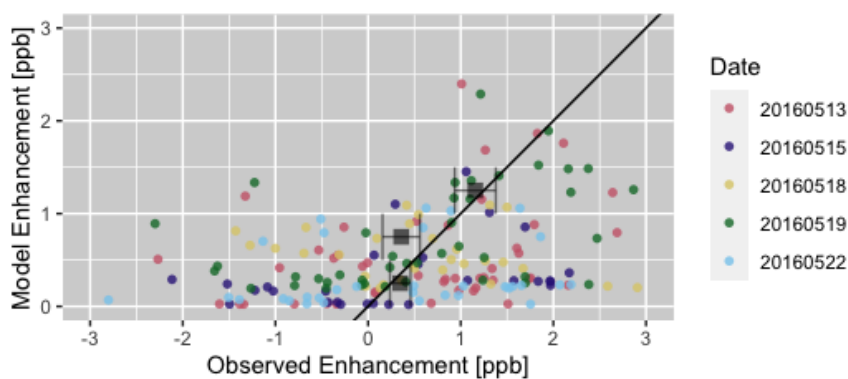
Figure 13. Optimized model correlation with the observations. The modeled background influence has been subtracted from both, showing just the enhancement in the total column due to local diffuse sources. The black line is a 1-1 line. These points represent one hour averages. Gray squares represent the mean observation values when model values are divided into 0.5 ppb wide bins. The horizontal error bars represent the sample standard deviations for each bin. The means of the first (0.0 - 0.5 ppb) and third (1.0 - 1.5 ppb) bins are significantly distinct ($p = 0.003$), demonstrating detection and quantification of the small enhancements in total column methane attributable specifically to diffuse emissions.

345   The background error, which was given an arbitrary large prior value of $\sigma_{bk} = 10$ ppb, was reduced to less than 1 ppb in the posterior for background times in the middle of the day (see Figure 14). This shows that that model was able to constrain this additional parameter in a meaningful way. Background values at the start and end of the day are less constrained, as their relative influence on the observations is smaller.
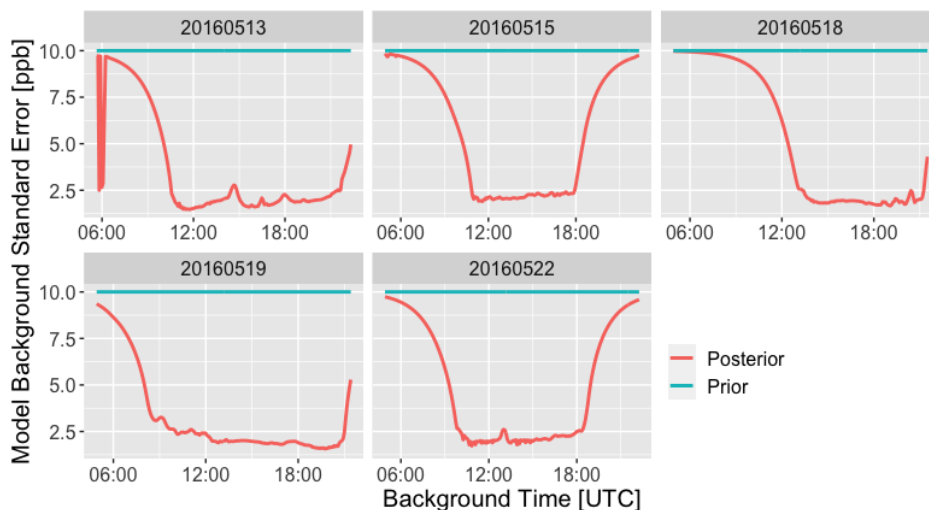
Figure 14. Posterior values for modeled background standard error.

    The effect of using different flux spatial distributions is shown in Figure 15. Using a distribution based on road density

350 resulted in diffuse emissions being scaled up by more than 500%, up to 301.4 ($\pm$ 70) $\mathrm{mol\,s^{-1}}$. This is because the road-based distribution shifted a large portion of emissions to roadways outside of the city center, lowering the prior emissions in the downtown area. The population-based distribution, while more similar to the HESTIA product, also shifted some of the emissions from downtown. The inversion using the population-based distribution increased diffuse emissions to 117.9 (± 28) $\mathrm{mol\,s^{-1}}$, higher than the HESTIA-based inversion (73.3 $\mathrm{mol\,s^{-1}}$) and the prior (43.4 $\mathrm{mol\,s^{-1}}$).

355   The results of this analysis are compared with other published results and bottom-up inventories in Figure 16. Not all of the inventories categorize emissions the same way, so the closest IPCC sector for each category was chosen for each inventory sector. Since this study is focused on diffuse emissions, the contributions from non-diffuse sources are taken directly from the prior.

4   Conclusions

360 We created a network of EM27/SUN spectrometers to enable distributed, efficient sampling of total column methane at high spatial resolution from the ground in and around the city of Indianapolis. Enhanced methane concentrations due to diffuse emissions from the urban core, likely from leaks and inefficiencies in the natural gas distribution system, were detected and quantified, distinct from methane originating from large identified point sources. Our observations suggest that the magnitude
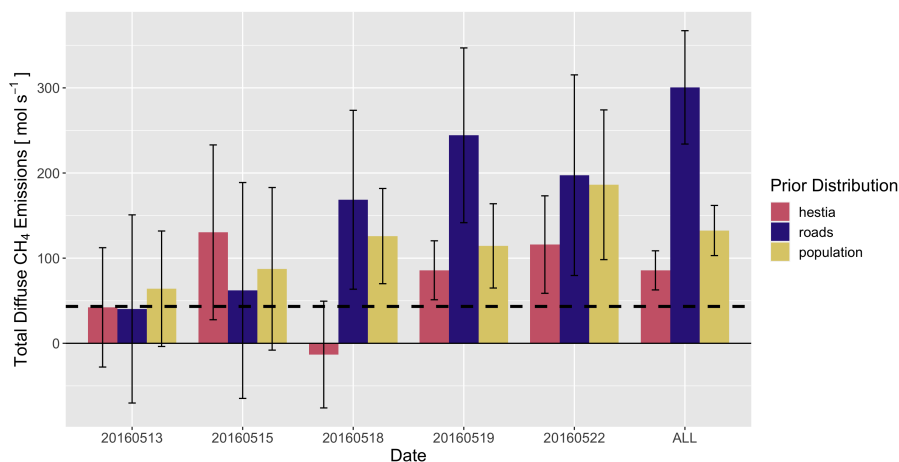
Figure 15. Total diffuse emissions from inversions using three different spatial distributions. The prior estimate of $43\,\mathrm{mol\,s^{-1}}$ is shown with a dashed line.

of diffuse emissions in notably larger than the values presented in bottom-up inventories. Our results are consistent with the independent analysis of data from tower-based sensors as shown in figure 16. Although our measurement and data analysis techniques are newer and not as established as the other method shown in 16, we believe that our result supports the findings shown in these other studies. Since all of these methods have different drawbacks and make different sets of assumptions, any attempt to truly quantify emissions from such a complex source should consider as many independent methods as possible.

Variations in the inversions results (Figure 15) between each day are quite large, but this is not surprising. Different days have significantly different wind patterns, which means different sections of the city are sampled on different days. If the inventory needs to be adjusted by different amounts for different sections of the domain, which is likely, the model will compute different scaling factors. By ingesting large amounts of data over a long time frame, covering many wind patterns, this issue can be resolved. Ideally, much more data than the five days used in this experimental study would be used.

Another improvement would be to solve for different scaling factors in different parts of the city. Theoretically, the inversion can solve for each grid square independently, with correlations between squares expressed in the co-variance matrices. However, in practice this requires significantly more observations, because the results become less constrained as the state vector increases in length. We believe that our framework could easily be expanded to spatially resolve emissions if implemented with data from a permanent or semi-permanent installation of sensors, such as MUCCNET ((Dietrich et al., 2020)).

Although this study uses only a few days of data, our results confirm the significance of diffuse methane emissions in urban areas. Even though the city of Indianapolis has relatively modern natural gas delivery systems, fugitive emissions represent more than half of all methane released into the atmosphere. This information is critical for those tasked with mitigating emissions, and suggests that increased investment in leak detection and repair efforts would make a measurable impact on the overall emission rate of a city. In order to assess the magnitude of diffuse methane emissions, and to measure the effect of
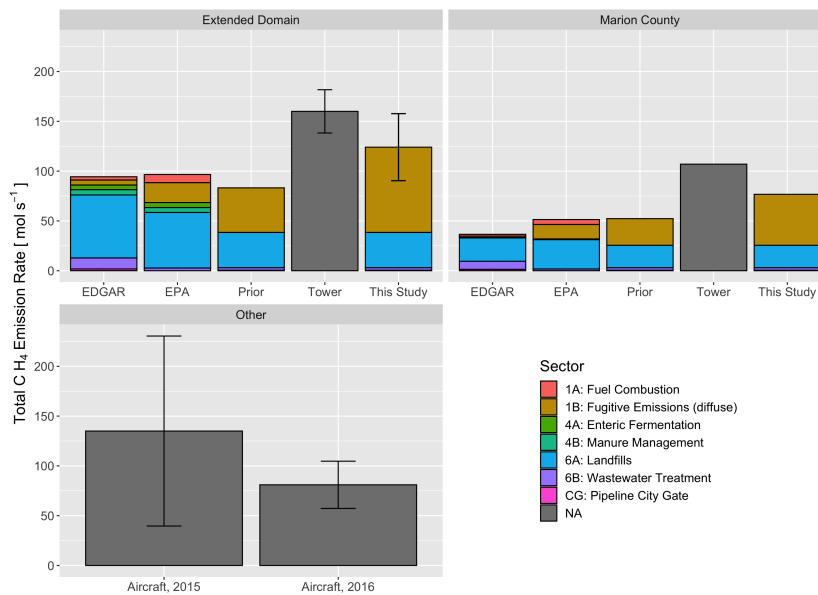
Figure 16. Comparison of total methane emissions estimates for the domain. The EPA inventory (0.01-degree resolution) (Maasakkers et al., 2016), and the EDGAR version 4.3 database (0.1-degree resolution) (European Commission, 2011) were interpolated to the domain. The emissions prior and tower inversion result are from a previous study (Lamb et al., 2016). These inventories were separated by IPCC emissions sectors (IPCC, 2006). Emissions from a smaller subset of the domain, that of Marion County, were also computed by scaling the emissions in that area by the posterior scaling factor. Emissions computed by using aircraft mass balance techniques (Cambaliza et al., 2015), which don't necessarily conform to either spatial domain, are also shown for comparison. Error bars for the tower and aircraft studies represent the reported 95% confidence intervals from their results. The error bars shown for this study represent the 95% confidence interval based on the posterior error variances.

mitigation efforts, more cities need to implement measurement networks like the one developed here, and maintain them for
385   long periods.

This work also highlights several factors which need to be carefully considered when designing a ground-based measurement network and accompanying model framework. For instance, an analysis of dominant wind conditions should be performed and sensor locations should be chosen so that there is minimal likelihood that sensors will observe intermittent point source influence. Alternatively, if the objective of the network is to quantify a point source, that likelihood should be maximized, as
390   intermittent influence would make that quantification more difficult. Furthermore, having portable sensors, like the EM27/SUN, allow different locations to be chosen on a daily basis to improve the quality of the measurement, if siting logistics are predetermined.

The characteristics of the inflowing (i.e. background) air are also of great importance, as hourly variations in background concentrations can be larger than the signal from the city itself. We present here a novel inversion framework that accounts
395   for the temporal variation of the background and determines the influence of the background concentrations at the measure-

ment points. We assume constant concentrations along the edge of the domain, which is reasonable in a city like Indianapolis, but would not be practical in other locations with complicated terrain, heterogeneous wind patterns, and strong upwind point sources. When designing a network and model framework, a background quantification technique which fits the specific conditions of the area of study should be chosen.

400   The spatial distribution of diffuse sources must also be carefully considered, as this can have large impacts on the inversion results, as shown in Figure 15. Although all three spatial distributions tested in this study suggest more emissions than present in the bottom-up inventory, the magnitudes differ significantly depending on how much weight is given to the core of the city. Distributing emissions based on road density resulted in a much larger posterior estimate than the other two methods because the road-based distribution shifts emissions from the center of the city to the suburbs, which are under-sampled by the net-

405 work. The inversion using the population-based distribution also suggests somewhat larger emissions than the HESTIA-based distribution because the population distribution does not account for emissions from commercial and industrial facilities concentrated in the core of the city. It is important to note that the inversion framework described here does not have a mechanism for incorporating spatial uncertainty and cannot redistribute emissions around the domain. Testing multiple plausible distributions gives a sense of the sensitivity of the model, and we suggest that any comprehensive analysis include model inversions

410 using several distributions.

    When an inversion is performed using the road-based distribution and all of the days of data, the estimate of emissions is much higher than any of the individual days. This is because the road-based distribution pulls emissions from the center of the city and puts them in the outer ring-roads, which have significantly less total footprint. This means that the product of the footprints and emissions grid is relatively low, and therefore the model gives more weight to the prior. Only when all of the

415 days are used is there enough data to influence the model significantly. Because the road-based distribution has relatively low prior emissions in the city center, the result is a large scaling factor. This also highlights the importance of sensor placement. Sensors should be placed close to the bulk of the suspected emissions sources so that strong influence is detected in a variety of wind conditions. If the experiment was designed with the road-based distribution in mind, sensors would be placed further apart in order to adequately sample the ring roads. We would also suggest that more sensors would be needed in this situation,

420 as a greater portion of emissions would be spaced out over a larger area.

    The size and shape of the domain must also be carefully chosen, as this will affect the ability of the model to correctly characterize inflowing air. The choice of domain can also affect the ability to compare the results to those of other studies, as shown in Figure 16, and consideration should be given to policy-relevant domains, such as city limits and county and state boundaries.

425   Future studies utilizing these types of instruments should also explore the trade-offs involved when choosing the number of sensors needed and their placement. While some studies have exploring this concept have been performed using similar footprint methods, they have mostly been done for in situ sensor networks ((Turner et al., 2018; Lopez-Coto et al., 2020), and total-column sensors require a different set of considerations. For instance, the footprints of total-column sensors are larger, which means fewer sensors are needed to sample the same area. Also, although portable FTIR systems may not be cheaper

430 than many in situ sensors, they do not require the presence of tall buildings or investment in tower infrastructure in order to be

deployed, which makes finding suitable deployment sites easier. Data collection with total-column systems is also dependent on direct sunlight, so any study exploring the utility of these types of networks in a specific region should also consider weather, solar angles, and shading.

As higher resolution satellites are developed to measure greenhouse gas emissions from complex sources, it is important to understand the magnitude and variation of total column concentrations on these scales. This work shows that in order to detect methane emissions from a source like the city of Indianapolis, an observing system must be able to accurately measure concentration gradients of less than 1 ppb in the total column. Furthermore, any such system must also have a method for discerning the influence of background methane concentrations. Although satellite observations will benefit from having spatially dense observations, sensors in low earth orbit are not likely to have good temporal resolution. This makes the identification of passing plumes even more difficult. Sensors like the EM27/SUN will likely provide complementary information and play an increasing role in the development, validation, and calibration of aircraft and satellite trace gas remote sensing missions. Conventional validations, such as comparisons to the few TCCON stations scattered throughout the globe, will be insufficient as these new sensors attempt to quantify small signals in complex situations. Although there are certainly trade-offs compared to tower-based in situ sensors (such as being limited to clear sky daylight hours), portable ground-based total column measurement systems have shown their usefulness as a component to a robust urban methane measurement network. As more and more cities seek to quantify their carbon emissions at policy relevant scales, it will be essential to employ innovative transport models and a diverse set of instruments, including ground based total column sensors.

5   Data and Code Availability

The data and inversion code used in this study is available at the Harvard Dataverse:

https://doi.org/10.7910/DVN/JWL4PK

6   Author Contribution

TJ, JF, JC, and SW designed the measurement campaign. TJ, JF, JC, HP, and MD performed the measurements. KH and PS provided and analysed aircraft data. EG processed campaign data. TJ, JC, FD, and CG designed the inversion framework. All authors contributed in writing the manuscript.

7   Competing Interests

The authors declare that they have no conflict of interest.

8 Acknowledgements

The authors would like to thank the University of Indianapolis for hosting this experiment and providing vital ground support. We would also like to thank Ludwig Heinle, Bruce Daube, John Budney, and Cody Floerchinger for their assistance with technical support, experimental design, and field measurements. We would like to thank the Environment Defense Fund for their financial support of this work. JC, FD, AW and JP acknowledge the financial support by the Deutsche Forschungsgemeinschaft (CH 1792/2-1; INST 95/1544) and Technical University of Munich – Institute for Advanced Study, funded by the German Excellence Initiative and the European Union Seventh Framework Program under grant agreement number 291763. HP and MKD thank the support by LANL's LDRD, NASA's Carbon Monitoring and UCOPs dairy methane emission projects.

460

References

Balashov, N., Davis, K., Miles, N., Lauvaux, T., Richardson, S., Barkley, Z., and Bonin, T.: Background heterogeneity and other uncertainties in estimating urban methane flux: Results from the Indianapolis Flux Experiment (INFLUX), Atmospheric Chemistry and Physics, 20, 4545–4559, https://doi.org/10.5194/acp-20-4545-2020, 2020.

Bergamaschi, P., Frankenberg, C., Meirink, J. F., Krol, M., Villani, M. G., Houweling, S., Frank, D., Edward, J. D., John, B. M., Luciana, V. G., Andreas, E., and Ingeborg, L.: Inverse modeling of global and regional CH_4 emissions using SCIAMACHY satellite retrievals, Journal of Geophysical Research Atmospheres, 114, https://doi.org/10.1029/2009JD012287, 2009.

Bonin, T. A., Carroll, B. J., Hardesty, R. M., Brewer, W. A., Hajny, K., Salmon, O. E., and Shepson, P. B.: Doppler lidar observations of the mixing height in Indianapolis using an automated composite fuzzy logic approach, Journal of Atmospheric and Oceanic Technology, 35, 473–490, https://doi.org/10.1175/JTECH-D-17-0159.1, 2018.

Bovensmann, H., Burrows, J. P., Buchwitz, M., Frerick, J., Noël, S., Rozanov, V. V., Chance, K. V., and Goede, A. P. H.: SCIA-MACHY: Mission Objectives and Measurement Modes, Journal of the Atmospheric Sciences, 56, 127–150, https://doi.org/10.1175/1520-0469(1999)056<0127:smoamm>2.0.co;2, 2002.

Brandt, A. R., Heath, G. A., Kort, E. A., O'Sullivan, F., Pétron, G., Jordaan, S. M., Tans, P., Wilcox, J., Gopstein, A. M., Arent, D., Wofsy, S., Brown, N. J., Bradley, R., Stucky, G. D., Eardley, D., and Harriss, R.: Energy and environment. Methane leaks from North American natural gas systems., Science (New York, N.Y.), 343, 733–5, https://doi.org/10.1126/science.1247045, http://www.ncbi.nlm.nih.gov/pubmed/24531957, 2014.

Butz, A., Dinger, A. S., Bobrowski, N., Kostinek, J., Fieber, L., Fischerkeller, C., Giuffrida, G. B., Hase, F., Klappenbach, F., Kuhn, J., Lübcke, P., Tirpitz, L., and Tu, Q.: Remote sensing of volcanic CO2, HF, HCl, SO2, and BrO in the downwind plume of Mt. Etna, Atmospheric Measurement Techniques, 10, 1–14, https://doi.org/10.5194/amt-10-1-2017, 2017.

Cambaliza, M. O. L., Shepson, P. B., Bogner, J., Caulton, D. R., Stirm, B., Sweeney, C., Montzka, S. A., Gurney, K. R., Spokas, K., Salmon, O. E., Lavoie, T. N., Hendricks, A., Mays, K., Turnbull, J., Miller, B. R., Lauvaux, T., Davis, K., Karion, A., Moser, B., Miller, C., Obermeyer, C., Whetstone, J., Prasad, K., Miles, N., and Richardson, S.: Quantification and source apportionment of the methane emission flux from the city of Indianapolis, Elementa: Science of the Anthropocene, 3, 000 037, https://doi.org/10.12952/journal.elementa.000037, https://www.elementascience.org/articles/10.12952/journal.elementa.000037, 2015.

Chen, J., Viatte, C., Hedelius, J. K., Jones, T., Franklin, J. E., Parker, H., Gottlieb, E. W., Wennberg, P. O., Dubey, M. K., and Wofsy, S. C.: Differential column measurements using compact solar-tracking spectrometers, Atmospheric Chemistry and Physics, https://doi.org/10.5194/acp-16-8479-2016, 2016.

Chen, J., Dietrich, F., Maazallahi, H., Forstmaier, A., Winkler, D., Hofmann, M. E., Van Der Gon, H. D., and Röckmann, T.: Methane emissions from the Munich Oktoberfest, Atmospheric Chemistry and Physics, 20, 3683–3696, https://doi.org/10.5194/acp-20-3683-2020, 2020.

Crosson, E. R.: A cavity ring-down analyzer for measuring atmospheric levels of methane, carbon dioxide, and water vapor, Applied Physics B: Lasers and Optics, 92, 403–408, https://doi.org/10.1007/s00340-008-3135-y, 2008.

Davis, K. J., Deng, A., Lauvaux, T., Miles, N. L., Richardson, S. J., Sarmiento, D. P., Gurney, K. R., Hardesty, R. M., Bonin, T. A., Brewer, W. A., Lamb, B. K., Shepson, P. B., Harvey, R. M., Cambaliza, M. O., Sweeney, C., Turnbull, J. C., Whetstone, J., and Karion, A.: The Indianapolis Flux Experiment (INFLUX): A test-bed for developing urban greenhouse gas emission measurements, Elem Sci Anth, 5, 21, https://doi.org/10.1525/elementa.188, 2017.

Dietrich, F., Chen, J., Voggenreiter, B., Aigner, P., Nachtigall, N., and Reger, B.: Munich permanent urban greenhouse gas column observing network, Atmospheric Measurement Techniques Discussions, p. in review, https://doi.org/10.5194/amt-2020-300, 2020.

Duren, R. M. and Miller, C. E.: Measuring the carbon emissions of megacities, Nature Climate Change, 2, 560–562, https://doi.org/10.1038/nclimate1629, http://dx.doi.org/10.1038/nclimate1629, 2012.

505

European Commission: Emission Database for Global Atmospheric Research (EDGAR), Tech. rep., 2011.

Fasoli, B., Lin, J. C., Bowling, D. R., Mitchell, L., and Mendoza, D.: Simulating atmospheric tracer concentrations for spatially distributed receptors: updates to the Stochastic Time-Inverted Lagrangian Transport model's R interface (STILT-R version 2), Geoscientific Model Development Discussions, pp. 1–19, https://doi.org/10.5194/gmd-2018-20, https://www.geosci-model-dev-discuss.net/gmd-2018-20/, 2018.

510

Frey, M., Sha, M. K., Hase, F., Kiel, M., Blumenstock, T., Harig, R., Surawicz, G., Deutscher, N. M., Shiomi, K., Franklin, J. E., Bösch, H., Chen, J., Grutter, M., Ohyama, H., Sun, Y., Butz, A., Mengistu Tsidu, G., Ene, D., Wunch, D., Cao, Z., Garcia, O., Ramonet, M., Vogel, F., and Orphal, J.: Building the COllaborative Carbon Column Observing Network (COCCON): Long-term stability and ensemble performance of the EM27/SUN Fourier transform spectrometer, Atmospheric Measurement Techniques, 12, 1513–1530, https://doi.org/10.5194/amt-12-1513-2019, 2019.

515

Garman, K., Hill, K., Wyss, P., Carlsen, M., Zimmerman, J., Stirm, B., Carney, T., Santini, R., and Shepson, P.: An airborne and wind tunnel evaluation of a wind turbulence measurement system for aircraft-based flux measurements, Journal of Atmospheric and Oceanic Technology, 23, 1696–1708, https://doi.org/10.1175/JTECH1940.1, 2006.

Gisi, M., Hase, F., Dohe, S., Blumenstock, T., Simon, A., and Keens, A.: XCO_2-measurements with a tabletop FTS using solar absorption spectroscopy, Atmospheric Measurement Techniques, 5, 2969–2980, https://doi.org/10.5194/amt-5-2969-2012, 2012.

520

Gurney, K., Romero-Lankao, P., Seto, K. C., Hutyra, L. R., Duren, R., Kennedy, C., Grimm, N. B., Ehleringher, J. R., Marcotullio, P., Hughes, S., Pincetl, S., Chester, M. V., Runfolo, D. M., Feddema, J. J., and Sperling, J.: Climate Change: Track Urban Emissions of a Human Scale, Nature, 525, 179–181, https://doi.org/10.1038/525179a, 2015.

Gurney, K. R., Razlivanov, I., Song, Y., Zhou, Y., Benes, B., and Abdul-Massih, M.: Quantification of fossil fuel CO_2 emissions on the building/street scale for a large U.S. City, Environmental Science and Technology, 46, 12 194–12 202, https://doi.org/10.1021/es3011282, 2012.

525

Hase, F., Frey, M., Blumenstock, T., Groß, J., Kiel, M., Kohlhepp, R., Mengistu Tsidu, G., Schäfer, K., Sha, M. K., and Orphal, J.: Application of portable FTIR spectrometers for detecting greenhouse gas emissions of the major city Berlin, Atmospheric Measurement Techniques, 8, 3059–3068, https://doi.org/10.5194/amt-8-3059-2015, 2015.

Hase, F., Frey, M., Kiel, M., Blumenstock, T., Harig, R., Keens, A., and Orphal, J.: Addition of a channel for XCO observations to a portable FTIR spectrometer for greenhouse gas measurements, Atmospheric Measurement Techniques, 9, https://doi.org/10.5194/amt-9-2303-2016, 2016.

530

Hedelius, J. K., Viatte, C., Wunch, D., Roehl, C. M., Toon, G. C., Chen, J., Jones, T., Wofsy, S. C., Franklin, J. E., Parker, H., Dubey, M. K., and Wennberg, P. O.: Assessment of errors and biases in retrievals of XCO_2, XCH_4, XCO, and XN_2O from a 0.5 cm-1 resolution solar-viewing spectrometer, Atmospheric Measurement Techniques, https://doi.org/10.5194/amt-9-3527-2016, 2016.

535

Hopkins, F. M., Ehleringer, J. R., Bush, S. E., Duren, R. M., Miller, C. E., Lai, C. T., Hsu, Y. K., Carranza, V., and Randerson, J. T.: Mitigation of methane emissions in cities: How new measurements and partnerships can contribute to emissions reduction strategies, Earth's Future, 4, 408–425, https://doi.org/10.1002/2016EF000381, 2016.

Hu, H., Landgraf, J., Detmers, R., Borsdorff, T., Aan de Brugh, J., Aben, I., Butz, A., and Hasekamp, O.: Toward Global Mapping of Methane With TROPOMI: First Results and Intersatellite Comparison to GOSAT, Geophysical Research Letters, 45, 3682–3689, https://doi.org/10.1002/2018GL077259, 2018.

IPCC: Guidelines for National Greenhouse Gas Inventories, in: The National Greenhouse Gas Inventories Programme, Hayama, Kanagawa, Japan, 2006.

Jacob, D. J., Turner, A. J., Maasakkers, J. D., Sheng, J., Sun, K., Liu, X., Chance, K., Aben, I., McKeever, J., and Frankenberg, C.: Satellite observations of atmospheric methane and their value for quantifying methane emissions, Atmospheric Chemistry and Physics, 16, 14 371–14 396, https://doi.org/10.5194/acp-16-14371-2016, 2016.

Janjic, Z. and Gall, R.: Scientific Documentation of the NCEP Nonhydrostatic Multiscale Model on the B grid (NMMB). Part 1 Dynamics, Ncar Tech. Note, pp. 1–80, papers://2ae67f3f-e008-4816-adce-b312905b08fd/Paper/p1066, 2012.

Kille, N., Baidar, S., Handley, P., Ortega, I., Sinreich, R., Cooper, O. R., Hase, F., Hannigan, J. W., Pfister, G., and Volkamer, R.: The CU mobile Solar Occultation Flux instrument: Structure functions and emission rates of NH_3, NO_2 and C_2H_6, Atmospheric Measurement Techniques, 10, 373–392, https://doi.org/10.5194/amt-10-373-2017, 2017.

Klappenbach, F., Bertleff, M., Kostinek, J., Hase, F., Blumenstock, T., Agusti-Panareda, A., Razinger, M., and Butz, A.: Accurate mobile remote sensing of XCO2 and XCH4 latitudinal transects from aboard a research vessel, Atmospheric Measurement Techniques, 8, 5023–5038, https://doi.org/10.5194/amt-8-5023-2015, 2015.

Kuze, A., Suto, H., Nakajima, M., and Hamazaki, T.: Thermal and near infrared sensor for carbon observation Fourier-transform spectrometer on the Greenhouse Gases Observing Satellite for greenhouse gas monitoring, Applied Optics, 48, 6716–6733, https://doi.org/10.1364/AO.48.006716, 2009.

Lamb, B. K., Cambaliza, M. O., Davis, K. J., Edburg, S. L., Ferrara, T. W., Floerchinger, C., Heimburger, A. M., Herndon, S., Lauvaux, T., Lavoie, T., Lyon, D. R., Miles, N., Prasad, K. R., Richardson, S., Roscioli, J. R., Salmon, O. E., Shepson, P. B., Stirm, B. H., and Whetstone, J.: Direct and Indirect Measurements and Modeling of Methane Emissions in Indianapolis, Indiana, Environmental Science and Technology, https://doi.org/10.1021/acs.est.6b01198, 2016.

Lin, J. C.: A near-field tool for simulating the upstream influence of atmospheric observations: The Stochastic Time-Inverted Lagrangian Transport (STILT) model, Journal of Geophysical Research, https://doi.org/10.1029/2002JD003161, 2003.

Lin, J. C. and Gerbig, C.: Accounting for the effect of transport errors on tracer inversions, Geophysical Research Letters, 32, 1–5, https://doi.org/10.1029/2004GL021127, 2005.

Lopez-Coto, I., Ren, X., Salmon, O. E., Karion, A., Shepson, P. B., Dickerson, R. R., Stein, A., Prasad, K., and Whetstone, J. R.: Wintertime CO2, CH4, and CO Emissions Estimation for the Washington, DC-Baltimore Metropolitan Area Using an Inverse Modeling Technique, Environmental Science and Technology, 54, 2606–2614, https://doi.org/10.1021/acs.est.9b06619, 2020.

Luther, A., Kleinschek, R., Scheidweiler, L., Defratyka, S., Stanisavljevic, M., Forstmaier, A., Dandocsi, A., Wolff, S., Dubravica, D., Wildmann, N., Kostinek, J., Jöckel, P., Nickl, A. L., Klausner, T., Hase, F., Frey, M., Chen, J., Dietrich, F., Necki, J., Swolkień, J., Fix, A., Roiger, A., and Butz, A.: Quantifying CH4 emissions from hard coal mines using mobile sun-viewing Fourier transform spectrometry, Atmospheric Measurement Techniques, 12, 5217–5230, https://doi.org/10.5194/amt-12-5217-2019, 2019.

Maasakkers, J. D., Jacob, D. J., Sulprizio, M. P., Turner, A. J., Weitz, M., Wirth, T., Hight, C., DeFigueiredo, M., Desai, M., Schmeltz, R., Hockstad, L., Bloom, A. A., Bowman, K. W., Jeong, S., and Fischer, M. L.: Gridded National Inventory of U.S. Methane Emissions, Environmental Science and Technology, https://doi.org/10.1021/acs.est.6b02878, 2016.

575 McKain, K., Down, A., Raciti, S. M., Budney, J., Hutyra, L. R., Floerchinger, C., Herndon, S. C., Nehrkorn, T., Zahniser, M. S., Jackson, R. B., Phillips, N., and Wofsy, S. C.: Methane emissions from natural gas infrastructure and use in the urban region of Boston, Massachusetts., Proceedings of the National Academy of Sciences of the United States of America, https://doi.org/10.1073/pnas.1416261112, 2015.

Miller, S. M., Wofsy, S. C., Michalak, A. M., Kort, E. A., Andrews, A. E., Biraud, S. C., Dlugokencky, E. J., Eluszkiewicz, J., Fischer, M. L.,
580 Janssens-Maenhout, G., Miller, B. R., Miller, J. B., Montzka, S. A., Nehrkorn, T., and Sweeney, C.: Anthropogenic emissions of methane in the United States, Proceedings of the National Academy of Sciences, 110, 20 018–20 022, https://doi.org/10.1073/pnas.1314392110, 2013.

Montzka, S. A., Dlugokencky, E. J., and Butler, J. H.: Non-CO 2 greenhouse gases and climate change, Nature, 476, 43–50, https://doi.org/10.1038/nature10322, http://dx.doi.org/10.1038/nature10322, 2011.

585 Parker, R., Boesch, H., Cogan, A., Fraser, A., Feng, L., Palmer, P. I., Messerschmidt, J., Deutscher, N., Griffith, D. W. T., Notholt, J., Wennberg, P. O., and Wunch, D.: Methane observations from the Greenhouse Gases Observing SATellite: Comparison to ground-based TCCON data and model calculations, Geophysical Research Letters, 38, 2–7, https://doi.org/10.1029/2011GL047871, 2011.

Peischl, J., Ryerson, T. B., Brioude, J., Aikin, K. C., Andrews, A. E., Atlas, E., Blake, D., Daube, B. C., De Gouw, J. A., Dlugokencky, E., Frost, G. J., Gentner, D. R., Gilman, J. B., Goldstein, A. H., Harley, R. A., Holloway, J. S., Kofler, J., Kuster, W. C., Lang, P. M., Novelli,
590 P. C., Santoni, G. W., Trainer, M., Wofsy, S. C., and Parrish, D. D.: Quantifying sources of methane using light alkanes in the Los Angeles basin, California, Journal of Geophysical Research Atmospheres, 118, 4974–4990, https://doi.org/10.1002/jgrd.50413, 2013.

Phillips, N. G., Ackley, R., Crosson, E. R., Down, A., Hutyra, L. R., Brondfield, M., Karr, J. D., Zhao, K., and Jackson, R. B.: Mapping urban pipeline leaks: Methane leaks across Boston, Environmental Pollution, 173, 1–4, https://doi.org/10.1016/j.envpol.2012.11.003, 2013.

Rodgers, C. D.: Inverse Methods for Atmospheric Sounding, World Scientific, Singapore, 2000.

595 Rosenzweig, C., Solecki, W., Hammer, S. A., and Mehrotra, S.: Cities_lead_the_way_in_climate.PDF, Nature, 7318, 909, 2010.

Sargent, M., Barrera, Y., Nehrkorn, T., Hutyra, L., Gately, C., Jones, T., McKain, K., Sweeney, C., Hegarty, J., Hardiman, B., and Wofsy, S.: Anthropogenic and biogenic CO $_2$ fluxes in the Boston urban region, Proceedings of the National Academy of Sciences of the United States of America, 115, https://doi.org/10.1073/pnas.1803715115, 2018.

Toja-Silva, F., Chen, J., Hachinger, S., and Hase, F.: CFD simulation of CO 2 dispersion from urban thermal power plant: Analysis of
600 turbulent Schmidt number and comparison with Gaussian plume model and measurements, Journal of Wind Engineering and Industrial Aerodynamics, 169, 177–193, https://doi.org/10.1016/j.jweia.2017.07.015, http://dx.doi.org/10.1016/j.jweia.2017.07.015, 2017.

Townsend-Small, A., Tyler, S. C., Pataki, D. E., Xu, X., and Christensen, L. E.: Isotopic measurements of atmospheric methane in Los Angeles, California, USA: Influence of "fugitive" fossil fuel emissions, Journal of Geophysical Research Atmospheres, 117, 1–11, https://doi.org/10.1029/2011JD016826, 2012.

605 Turner, A. J., Jacob, D. J., Benmergui, J., Brandman, J., White, L., and Randles, C. A.: Assessing the capability of different satellite observing configurations to resolve the distribution of methane emissions at kilometer scales, Atmospheric Chemistry and Physics, 18, 8265–8278, https://doi.org/10.5194/acp-18-8265-2018, 2018.

Turner, A. J., Frankenberg, C., and Kort, E. A.: Interpreting contemporary trends in atmospheric methane, Proceedings of the National Academy of Sciences of the United States of America, 116, 2805–2813, https://doi.org/10.1073/pnas.1814297116, 2019.

610 Van Der Hoven, I.: Power Spectrum of Horizontal Wind Speed in the Frequency Range from 0.0007 to 900 Cycles per Hour, Journal of Meteorology, 14, 160–164, 1957.

Veefkind, J. P., Aben, I., McMullan, K., Förster, H., de Vries, J., Otter, G., Claas, J., Eskes, H. J., de Haan, J. F., Kleipool, Q., van Weele, M., Hasekamp, O., Hoogeveen, R., Landgraf, J., Snel, R., Tol, P., Ingmann, P., Voors, R., Kruizinga, B., Vink, R., Visser, H., and Levelt, P. F.: TROPOMI on the ESA Sentinel-5 Precursor: A GMES mission for global observations of the atmospheric composition for climate, air quality and ozone layer applications, Remote Sensing of Environment, 120, 70–83, https://doi.org/10.1016/j.rse.2011.09.027, http://dx.doi.org/10.1016/j.rse.2011.09.027, 2012.

Viatte, C., Lauvaux, T., Hedelius, J. K., Parker, H., Chen, J., Jones, T., Franklin, J. E., Deng, A. J., Gaudet, B., Verhulst, K., Duren, R., Wunch, D., Roehl, C., Dubey, M. K., Wofsy, S., and Wennberg, P. O.: Methane emissions from dairies in the Los Angeles Basin, Atmospheric Chemistry and Physics, https://doi.org/10.5194/acp-17-7509-2017, 2017.

Von Fischer, J. C., Cooley, D., Chamberlain, S., Gaylord, A., Griebenow, C. J., Hamburg, S. P., Salo, J., Schumacher, R., Theobald, D., and Ham, J.: Rapid, Vehicle-Based Identification of Location and Magnitude of Urban Natural Gas Pipeline Leaks, Environmental Science and Technology, 51, 4091–4099, https://doi.org/10.1021/acs.est.6b06095, 2017.

Wennberg, P. O., Gaudet, B., Parker, H., Duren, R., Wofsy, S., Verhulst, K., Deng, A. J., Chen, J., Roehl, C., Lauvaux, T., Viatte, C., Hedelius, J. K., Jones, T., Franklin, J. E., Dubey, M. K., and Wunch, D.: Methane emissions from dairies in the Los Angeles Basin, Atmospheric Chemistry and Physics, 17, 7509–7528, https://doi.org/10.5194/acp-17-7509-2017, 2017.

Wu, D., Lin, J. C., Oda, T., Ye, X., Lauvaux, T., Yang, E. G., and Kort, E. A.: A Lagrangian Approach Towards Extracting Signals of Urban CO 2 Emissions from Satellite Observations of Atmospheric Column CO 2 (XCO 2): X-Stochastic Time-Inverted Lagrangian Transport model (" X- STILT v1 . 1 "), pp. 1–43, 2018.

Wunch, D., Toon, G. C., Blavier, J. F. L., Washenfelder, R. A., Notholt, J., Connor, B. J., Griffith, D. W., Sherlock, V., and Wennberg, P. O.: The total carbon column observing network, Philosophical Transactions of the Royal Society A: Mathematical, Physical and Engineering Sciences, 369, 2087–2112, https://doi.org/10.1098/rsta.2010.0240, 2011.

Zhou, M., Langerock, B., Vigouroux, C., Sha, M. K., Ramonet, M., Delmotte, M., Mahieu, E., Bader, W., Hermans, C., Kumps, N., Metzger, J. M., Duflot, V., Wang, Z., Palm, M., and De Mazière, M.: Atmospheric CO and CH 4 time series and seasonal variations on Reunion Island from ground-based in situ and FTIR (NDACC and TCCON) measurements, Atmospheric Chemistry and Physics, 18, 13 881–13 901, https://doi.org/10.5194/acp-18-13881-2018, 2018.